SUPPLEMENTARY INFORMATION

Data Analysis Supplement

METHOD

Gravitational waves stretch and compress the spatial dimensions perpendicular to the direction of wave propagation. In a Michelson interferometer with suspended mirrors, the gravitational wave would cause stretching and shrinking of orthogonal arms, as shown in Figure 1, which would result in corresponding fluctuations in the laser intensity at the output of the interferometer. Hence, transient or periodic gravitational waves would cause transient or periodic fluctuations in the output laser power. A stochastic gravitational-wave background (SGWB) signal would cause random fluctuations in output laser power, which are indistiguishable from various instrumental noise sources. We hence search for a SGWB by cross-correlating strain data from pairs of interferometers, as described in [8]. In particular, we define the following cross-correlation estimator:

$$Y = \int_0^{+\infty} df \ Y(f) \tag{1}$$
$$= \int_{-\infty}^{+\infty} df \int_{-\infty}^{+\infty} df' \ \delta_T(f-f') \ \tilde{s}_1(f)^* \ \tilde{s}_2(f') \ \tilde{Q}(f'),$$

where δ_T is a finite-time approximation to the Dirac delta function, $\tilde{s}_1$ and $\tilde{s}_2$ are the Fourier transforms of the strain time-series of two interferometers, and $\tilde{Q}$ is a filter function. Assuming that the detector noise is Gaussian, stationary, uncorrelated between the two interferometers, and much larger than the GW signal, the variance of the
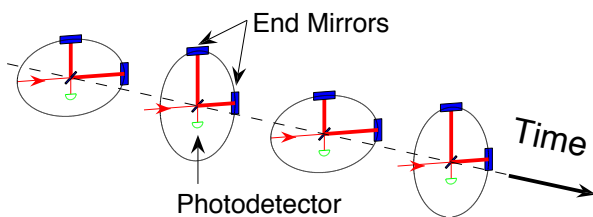

FIG. 1: **Effect of a gravitational wave on an interferometer.** A gravitational wave traveling perpendicular to the plane of the interferometer stretches and compresses interferometer arms in an alternating manner. The laser beam (entering from the left) is split equally between the arms, the two new beams travel to and reflect back from the end mirrors, and are superposed at the photo-detector (at the bottom). Changes in the arm lengths cause the two beams to acquire different phases while traveling in the arms, the differential component of which is observed as modulations in the laser light intensity at the photo-detector.

estimator Y is given by:

$$\sigma_Y^2 = \int_0^{+\infty} df \ \sigma_Y^2(f)$$
$$\approx \frac{T}{2} \int_0^{+\infty} df P_1(f) P_2(f) \mid \tilde{Q}(f) \mid^2, \tag{2}$$

where $P_i(f)$ are the one-sided strain power spectral densities (PSDs) of the two interferometers and T is the measurement time. Optimization of the signal-to-noise ratio leads to the following form of the optimal filter [8]:

$$\tilde{Q}(f) = \mathcal{N} \ \frac{\gamma(f)\Omega_{\mathrm{GW}}(f)H_0^2}{f^3 P_1(f)P_2(f)} \ , \tag{3}$$

where H_0 is the present value of the Hubble parameter, assumed below to take the value $H_0 = 72$ km/s/Mpc [19], and $\gamma(f)$ is the overlap reduction function [8], arising from the overlap of antenna patterns of interferometers at different locations and with different orientations. For the Hanford-Livingston pairs the sensitivity above 50 Hz is attenuated due to the overlap reduction, while the identical antenna patterns of the colocated Hanford interferometers imply $\gamma(f) = 1$. Hence, the colocated Hanford interferometer pair is more sensitive to the isotropic SGWB than the Hanford-Livingston pairs, but it is also more susceptible to environmental and instrumental correlations. For this reason, this pair is not included in the analysis presented here. Since most theoretical models in the LIGO frequency band are characterized by a power law spectrum, we assume a power law template GW spectrum with index α,

$$\Omega_{\mathrm{GW}}(f) = \Omega_\alpha \left(\frac{f}{100 \ \mathrm{Hz}}\right)^\alpha. \tag{4}$$

The normalization constant $\mathcal{N}$ in Equation 3 is chosen such that $< Y >= \Omega_\alpha$.

RESULTS

Our results are based on the LIGO data acquired during the science run S5, which took place between November 5, 2005 and September 30, 2007. Virgo [19] and GEO [20] detectors were also operating during some parts of this science run. However, due to their lower strain sensitivities around 100 Hz, these interferometers were not included in the search presented here. We analyzed the H1-L1 and H2-L1 interferometer pairs. The data for each interferometer pair was divided into 60 sec segments, downsampled to 1024 Hz, and high-pass filtered with a 6th order Butterworth filter with 32 Hz knee frequency. Each
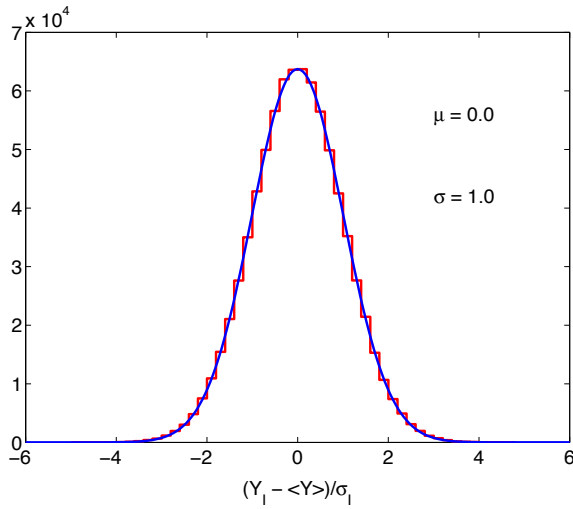
FIG. 2: Histogram of the fluctuations of the estimator Y_I over segments I around the mean, normalized by the standard deviation σ_I is shown in red (for the H1-L1 pair). The blue curve shows the Gaussian fit to the histogram, which has zero mean and unit variance. The Kolmogorov-Smirnov test statistic (comparing the histogram and the fit) is 0.2 for H1-L1 (0.4 for H2-L1), indicating that the data is indeed Gaussian-distributed, and that the estimate of the theoretical variance σ_I^2 is reliable.

segment I was Hann-windowed and estimators $Y_I(f)$ and $\sigma_I(f)$ were evaluated with 0.25 Hz resolution. To recover the loss of signal-to-noise due to Hann-windowing, segments were 50% overlapped. A weighed average was performed over all segments from both interferometer pairs, with inverse variances as weights.

The data were preselected to avoid digitizer saturation effects, periods with unreliable calibration, and periods suffering from known instrumental transient disturbances. In addition, about 3% of the segments were found to deviate from the assumption of stationary noise: the difference between σ_I and σ calculated using the neighboring segments exceeded 20% for these segments, and they were not included in the analysis. The 20% threshold is optimal as it yields gaussian distribution of the data (c.f. Figure 2), while minimizing the amount of eliminated data. The data quality selection was performed blindly, using an un-physical 0.5-sec time-shift between the two interferometers (a broadband SGWB covering the range of $\sim$ 100 Hz is expected to have coherence time $\sim$ 10 ms, as also depicted in Figure 5). Once the data selection was completed, the final zero-lag analysis was performed. The selected segments amount to 292 days of exposure time for H1-L1 (294 days for H2-L1).

To identify potentially contaminated frequency bins, we calculated the coherence between H1 and L1 (and H2 and L1) over the entire S5 run. The coherence is defined
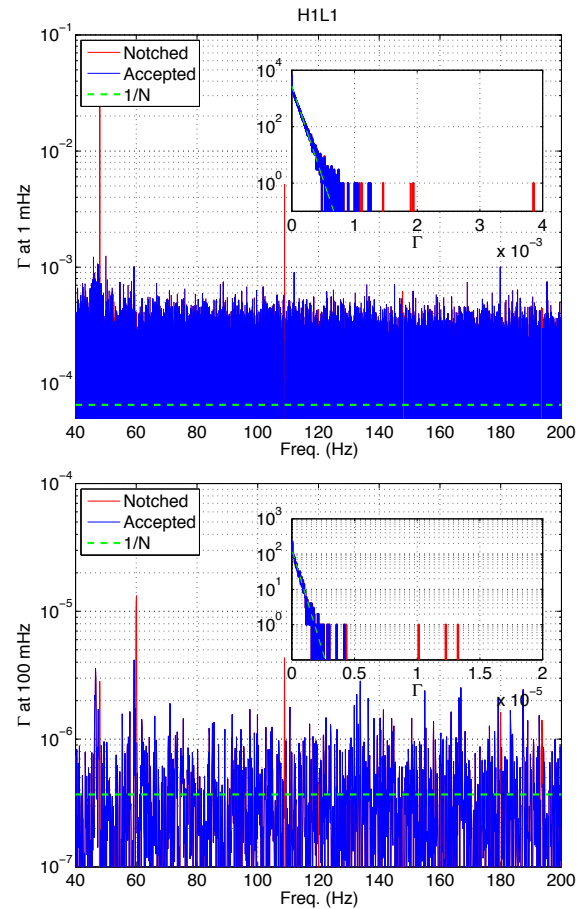

FIG. 3: Coherence between H1 and L1 strain data is shown at 1 mHz resolution (top) and 100 mHz resolution (bottom). The insets show the histograms of the coherence along with the expected exponential distribution. Note that after notching the contaminated bins (red), the remaining frequencies follow the expected exponential distribution. Note: N denotes the number of averages used in the calculation.

as

$$\Gamma(f) = \frac{|\langle P_{12}(f)\rangle|^2}{\langle P_1(f)\rangle\langle P_2(f)\rangle}, \qquad (5)$$

where $\langle P_{12}(f)\rangle$ is the average strain cross-spectral density between two interferometers and $\langle P_i(f)\rangle$ is the average strain power-spectral density for the interferometer i. These calculations have revealed several instrumentally correlated lines between each pair of interferometers: 16 Hz harmonics (associated with the data acquisition clock), 60 Hz harmonics (AC power line), and injected simulated pulsar signals (52.75 Hz, 108.75 Hz, 148 Hz, 193.5 Hz, and 265.5 Hz). These lines were found to be correlated between instruments in the blind analysis, and were excluded from the final zero-lag analysis.
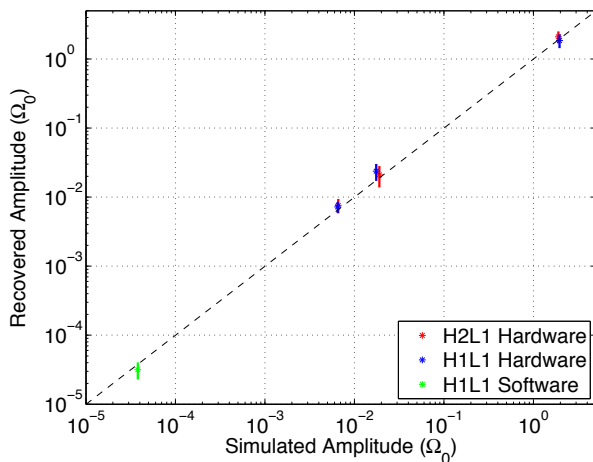
FIG. 4: Stochastic signal simulations in hardware for H1-L1 (blue) and H2-L1 (red), and in software (H1-L1, green) are shown. The error bars denote 2σ ranges.
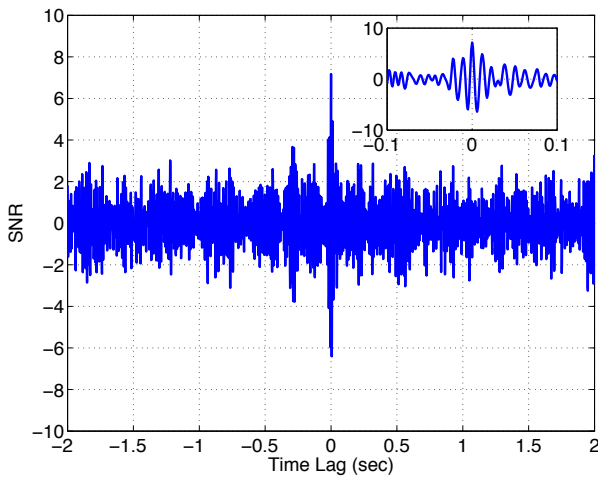

FIG. 5: Signal-to-noise ratio for the recovery of a software simulation with H1-L1 data with $\Omega_0^{simulated} = 3.8 \times 10^{-5}$ is shown as a function of the time-lag between the two interferometers. The inset shows the zoom-in around zero-lag: the signal is recovered well for zero-lag (SNR ≈ 7.2), but it disappears quickly with time-lag of ± 30 ms.
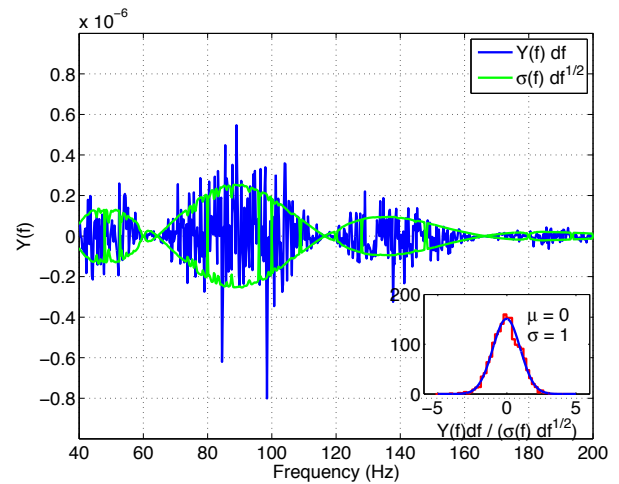

FIG. 6: $Y(f)$ and $\sigma(f)$ obtained by combining the H1-L1 and H2-L1 data from the S5 run. The inset shows that the ratio of the two spectra is consistent with a Gaussian of zero mean and unit variance.
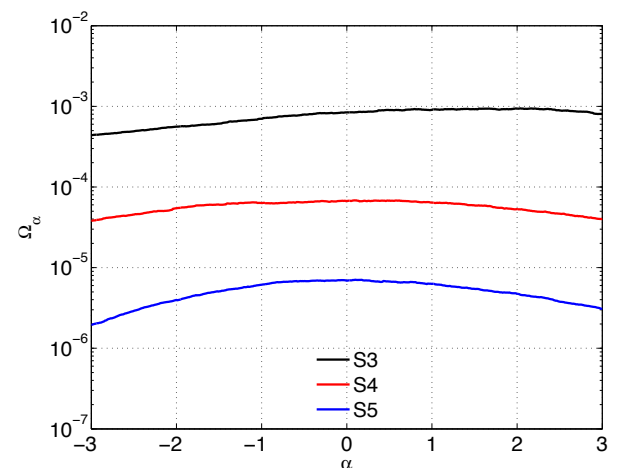

FIG. 7: Upper limit is shown as a function of the power index α for several LIGO results: based on the previous runs S3 and S4 and the S5 result presented here.

Figure 3 shows the coherence between H1 and L1 strain data at 1 mHz and 100 mHz resolutions.

The search algorithm described here is verified using signal simulations. The simulations are performed in hardware (by physically moving the interferometer mirrors coherently between interferometers), in which case they are short in duration and strong in amplitude. They are also performed in software, by adding the stochastic signal to the interferometer data, in which case they can be long in duration and relatively weak in amplitude. Three hardware simulations were performed, with amplitudes of $\Omega_0 \approx 2$ (20 min long), 2×10^{-2} (20 min long), and

6.5×10^{-3} (~ 3.8 hours long) and they were successfully recovered (within experimental uncertainties) for both H1-L1 and H2-L1 pairs. A software simulation was performed and successfully recovered using about $1/2$ of the H1-L1 data, with the amplitude of $\Omega_0 = 3.8 \times 10^{-5}$. Figures 4 and 5 demonstrate the recovery of both hardware and software simulations.

We apply the above search technique to the data acquired by LIGO during the science run S5, repeating it for the interferometer pairs H1-L1 and H2-L1. We treat the data from the two pairs as uncorrelated, although H1 and H2 are known to suffer from instrumental and environmental correlations. We have verified

that the level of the H1-H2 correlations is sufficiently small that it could affect the result presented here by less than 1%. The resulting composite spectrum for the frequency independent template ($\alpha = 0$) is shown in Figure 6. Integrated over the frequency band 41.5-169.25 Hz, which contains 99% of the sensitivity as determined by the variance integrand, this leads to the final point estimate for the frequency independent GW spectrum: $\Omega_0 = (2.1 \pm 2.7) \times 10^{-6}$, where the quoted error is statistical. We calculate the Bayesian posterior distribution for Ω_0 using this result. For the prior distribution of Ω_0 we use our previously published posterior distribution from the earlier S4 run [22]. We also marginalize over the calibration uncertainty, which is the dominant systematic error in this analysis and was estimated to be 13.4% for L1 and 10.3% for H1 and H2. With these assumptions, the final 95% confidence upper limit is $\Omega_0 < 6.9 \times 10^{-6}$. Figure 7 shows the 95% confidence upper limit as a function of the power index α of the template spectrum. This result is more than an order of magnitude improvement over the latest LIGO result in this frequency region [22].

OUTLOOK

LIGO and Virgo are planning significant upgrades to their interferometers, known as Advanced LIGO and Advanced Virgo. These upgrades will improve the interferometers' strain sensitivities by 10 times across the entire frequency band, and they will extend the sensitive frequency band down to ~ 10 Hz. Consequently, the network of advanced detectors will be able to probe the isotropic SGWB at the level of $\Omega_{GW} \sim 10^{-9}$ or better. Moreover, while searches for isotropic SGWB tend to be dominated by pairs of nearby or co-located detectors, the presence of the third location in the network is crucial for searches for non-isotropic SGWB. Hence, the network of advanced detectors is expected to produce detailed maps of the gravitational-wave sky, potentially revealing non-isotropic sources of SGWB, such as point sources or sources distributed in the galactic plane. Techniques for performing the searches for non-isotropic SGWB are currently under development.

Author Contributions: The LIGO Scientific Collaboration (LSC) and the Virgo Collaboration are organized into several working groups, each focusing on a different aspect of the experiment. Each author is associated with one or more of these groups. Moreover, all of the authors participated in the acquisition of the data that led to this letter. As described in the MoU between the LSC and Virgo, there are joint data analysis groups: the Burst Search Group (chairs E. Katsavounidis, P. Shawhan and P.Hello) performs searches for transient signals; the Compact Binary Coalescences Search Group (chairs S. Fairhurst, A. Weinstein and F. Marion) performs searches for compact binary coalescence signals; the Continuous-Waves Search Group (chairs K. Riles, G. Woan and C. Palomba) performs searches for continuous periodic signals; the Stochastic Search Group (chairs S. Ballmer, V. Mandic and G. Cella) performs searches for stochastic signals and is responsible for the analysis that led to the result presented here and for writing of this letter. The Stochastic Review Committee (chairs W. Anderson and F. Ricci) has conducted an extensive internal review of the method and the results presented in this letter. Similar review committees exist for the Burst, Compact Binary Coalescences, and Continuous-Waves groups. The Data Analysis Council (chairs M.A. Papa and G. Guidi) coordinates different analysis efforts. On the LIGO side the Detector Characterization Group (chair G. Gonzalez) performs studies of LIGO detector performance; Calibration Group (chairs K. Kawabe and X. Siemens) establishes the calibration of LIGO detectors. On the Virgo side the Reconstruction group (coordinator L. Rolland) provides a reconstructed and calibrated strain measurement while the Noise Study group (coord. E. Cuoco) studies the noise present in the detector. The Commissioning group (coord. E. Calloni) establishes proper detector tuning. The Detector Group (coord. P. Rapagnani) organizes detector operations and upgrades. The Director of the LIGO Laboratory is J. Marx, the Deputy Director is A. Lazzarini, and the LSC spokesperson is D. Reitze. The Virgo Spokesperson is F. Fidecaro.